

Characterization of TiO_2 And An As-Prepared TiO_2/SiO_2 Composite And Their Photocatalytic Performance For The Reduction Of Low-Concentration $N-NO_3^-$ In Water

Wanzhen Zhong

Shandong Agricultural University

Weizhang Fu (✉ sdaufwz@sdau.edu.cn)

Shandong Agricultural University <https://orcid.org/0000-0002-2629-1091>

Shujuan Sun

Shandong Agricultural University

Lingsheng Wang

Shandong Agricultural University

Huaihao Liu

Shandong Agricultural University

Junzhi Wang

Qingdao University of Technology

Research Article

Keywords: low-concentration $N-NO_3^-$, TiO_2 , TiO_2/SiO_2 , Photocatalysis, Reduction reaction, Nitrogen conversion rate

Posted Date: December 14th, 2021

DOI: <https://doi.org/10.21203/rs.3.rs-1027427/v1>

License:   This work is licensed under a Creative Commons Attribution 4.0 International License.

[Read Full License](#)

1 **Characterization Of TiO₂ And An As-Prepared TiO₂/SiO₂ Composite And Their**
2 **Photocatalytic Performance For The Reduction Of Low-Concentration N-NO₃⁻**
3 **In Water**

4 *Environmental Science and Pollution Research*

5 Wanzhen Zhong^{1,2}, Weizhang Fu*¹, Shujuan Sun*¹, Lingsheng Wang¹, Huaihao Liu¹, Junzhi
6 Wang²

7 1. College of Resources and Environment, Shandong Agricultural University, Tai'an, 271018, PR
8 China

9 2. School of Environmental and Municipal Engineering, Qingdao University of Technology,
10 Qingdao 266000, China

11 Wanzhen Zhong E-mail: 96359065@qq.com

12 Shujuan Sun E-mail: sunsjnk@sdau.edu.cn

13 Lingsheng Wang E-mail: 1195443917@qq.com

14 Huaihao Liu E-mail: 248211573@qq.com

15 Junzhi Wang E-mail: gualk1009@hotmail.com

16 * Co-corresponding author:

17 Weizhang Fu; Phone No.: +8613905383700; E-mail: sdaufwz@sdau.edu.cn

18 **Abstract:**Excessive N-NO_3^- water pollution has become a widespread and serious problem that
19 threatens human and ecosystem health. Here, a $\text{TiO}_2/\text{SiO}_2$ composite photocatalyst was prepared via the
20 sol-gel/hydrothermal method. TiO_2 and $\text{TiO}_2/\text{SiO}_2$ were characterized by X-ray diffraction (XRD),
21 UV-Vis differential reflectance spectroscopy (DRS), Fourier infrared (FT-IR) spectroscopy, X-ray
22 photoelectron spectroscopy (XPS), scanning electron microscopy (SEM), and energy-dispersive X-ray
23 spectroscopy (EDS). Afterward, the photocatalytic performance of TiO_2 and $\text{TiO}_2/\text{SiO}_2$ to reduce low
24 nitrate concentrations ($30 \text{ mgN}\cdot\text{L}^{-1}$) under UV light were evaluated and the effects of different factors
25 on this process were investigated, after which the reaction conditions were optimized. Removal rates of
26 up to 99.93% were achieved at a hole scavenger (formic acid) concentration of $0.6 \text{ mL}\cdot\text{L}^{-1}$, a CO_2 flow
27 rate of $0.1 \text{ m}^3\cdot\text{h}^{-1}$, and a TiO_2 concentration of $0.9 \text{ g}\cdot\text{L}^{-1}$. In contrast, $\text{TiO}_2/\text{SiO}_2$ at a $1.4 \text{ g}\cdot\text{L}^{-1}$
28 concentration and a TiO_2 load rate of 40% achieved a removal rate of 83.48%,But with more than 98%
29 of nitrogen generation rate. NO_2^- and NH_4^+ were the minor products, whereas N_2 was the main product.

30 **Keywords:** low-concentration N-NO_3^- ; TiO_2 ; $\text{TiO}_2/\text{SiO}_2$; Photocatalysis; Reduction reaction;
31 Nitrogen conversion rate

32 1 Introduction

33 Water is a vital and often limiting resource for the development of human society. Urban sewage
34 seepage, industrial wastewater infiltration, agricultural pesticides, and fertilizer application all
35 contribute greatly to the exacerbation of N-NO_3^- groundwater pollution, and this has become a serious
36 environmental issue worldwide. In addition to being chemically stable, N-NO_3^- is highly water-soluble
37 and mobile, making it difficult to remove from water environments (Velu et al. 2021). This compound
38 poses a serious risk to human and environmental health and has been linked to teratogenicity and
39 carcinogenicity, in addition to the eutrophication of water bodies and land salinization (Ghafari et al.
40 2008, Tugaoen et al. 2017). Therefore, N-NO_3^- is not only considered an indicator of conventional
41 water quality but is also classified as a toxicological indicator. According to the World Health

42 Organization and the European Union, the concentration of N-NO₃⁻ in drinking water should not exceed
43 10 and 11.3 mg/L, respectively.

44 Biological denitrification, a common water treatment method, requires the introduction of a carbon
45 source, and the temperature and carbon to nitrogen ratio of this reaction must be carefully controlled
46 (Yao et al. 2020). Further, the rapid aging of ion exchange membranes for physicochemical
47 denitrification leads to high costs and, in addition to not fully removing nitrate, this method produces
48 high concentrations of saline wastewater (Gao et al. 2019). Moreover, the reaction conditions of
49 chemical reductive denitrification cannot be easily controlled and are prone to hydrogen and oxygen
50 evolution and other side reactions, resulting in secondary environmental pollution (Garcia-Segura et al.
51 2018). In contrast, photocatalysis by semi-conductors is a novel and environmentally friendly method
52 for N-NO₃⁻ removal that is highly selective toward N₂, has fast reduction kinetics and a small footprint,
53 and does not generate sludge.

54 Velu *et al.* (2021) reported N-NO₃⁻ removal rates of up to 94% via photocatalysis using an
55 Al₂O₃/MOGAC nano-composite. Li *et al.* (2021) degraded 50 mg·L⁻¹ N-NO₃⁻ with 1% Fe-LNO under
56 UV light. After 120 min, the optimized nitrate removal rate reached 86.69% and the optimized N₂
57 selectivity was 85.71%. Bi *et al.* (2021) evaluated the degradation of nitrogen oxide catalyzed by
58 TiO₂/0.25Nb₂O₅ under visible light and achieved a removal rate of 77.23% . Liu et al. (2021) reported
59 that Ag₃Pd₇/g-C_{1.95}N₄ exhibited the highest photocatalytic activity and selectivity for the photocatalytic
60 reduction of NO₃⁻ and NO₂⁻ under 25 °C and 365 nm irradiation, and the removal rates of NO₃⁻ and
61 NO₂⁻ were 87.4% and 61.8%, respectively. Hou *et al.* (2021) prepared 5 wt% Ag/SiO₂@cTiO₂ and
62 reported that the nitrate removal rate and N₂ selectivity were respectively 95.8% (C₀ = 2000 mg/L) and
63 93.6% after 4 h. Wang *et al.*(2021) prepared 10 wt% SiW₉/TiO₂/Cu and reported that the N-NO₃⁻ (C₀=
64 30 mgN/L) removal rate and the N₂ selectivity were respectively 76.53% and 82.09% after UV
65 radiation for 6 h.

66 TiO₂ has good photo-responsive performance with a band gap energy of 3.2 eV and can utilize
67 radiation with wavelengths less than 390 nm. TiO₂ becomes excited when it is irradiated with light at
68 wavelengths higher than its band gap energy, after which the excited electrons (e⁻) in the valence band
69 migrated to the conduction band. This process forms highly active negatively charged electrons and
70 leaves positively charged holes (h⁺) in the valence band, resulting in electron-hole pairs. The resulting

71 electrons and holes are strong oxidizing and reducing agents, which can degrade many pollutants when
72 irradiated with light (Lv et al. 2019). In addition to its excellent optical properties, TiO₂ has become a
73 popular catalyst for the photocatalytic reduction of N-NO₃⁻ due to its non-toxicity, stability, and low
74 cost (Li et al. 2019, Tsang et al. 2019, Yang et al. 2004).

75 For water treatment purposes, TiO₂ must be easily separated and recovered. Therefore, this
76 compound is routinely modified by coating and is immobilized on a substrate to separate it from the
77 treated water more effectively (Woottikrai et al. 2022). Typical coating modification methods mainly
78 include electrochemical, hydrothermal, sol-gel, and chemical precipitation methods, among which the
79 sol-gel method is the most common.

80 Therefore, this study assessed the photocatalytic treatment of low N-NO₃⁻ concentrations in water
81 using TiO₂. Further, to recycle the TiO₂, a sol-gel method was used to coat and immobilize it on SiO₂ to
82 obtain a TiO₂/SiO₂ composite catalyst. Particularly, three aspects were systematically evaluated in this
83 study: (a) the effects of different factors (catalyst dose, catalyst loading rate, hole scavenger dose, and
84 type of shielding gas) on the photocatalytic degradation of N-NO₃⁻, (b) catalyst stability, and (c) the
85 mechanism of photocatalytic reduction of N-NO₃⁻ by TiO₂ and the TiO₂/SiO₂ composite.

86 **2 Materials and methods**

87 In addition to TiO₂ nanoparticles, this study also evaluated a TiO₂/SiO₂ composite by loading
88 different proportions of TiO₂ on the surface of SiO₂ particles. The photocatalytic reduction of N-NO₃⁻
89 under UV light was simulated indoors.

90 **2.1 Preparation of the TiO₂/SiO₂ composite catalyst**

91 SiO₂ particles were immersed in a NaOH solution (pH = 10) and sonicated for 2 h to increase their
92 surface roughness. Nanoparticle composites were generated using the sol-gel hydrothermal synthesis
93 method (Jesus et al. 2021, Takari et al. 2021, Wang et al. 2017). Solution A was prepared by slowly
94 adding 10 mL of butyl titanate to 20 mL of absolute ethanol, followed by 1.8 mL of glacial acetic acid
95 while constantly stirring the mixture. Solution B was prepared by mixing 20 mL of absolute ethanol
96 with 2 mL of distilled water. Solution B was then added drop by drop to A solution with rapid stirring
97 and butyl titanate was slowly hydrolyzed with continued stirring until it formed a solvate. Different
98 amounts of SiO₂ particles were added and sonicated to further hydrolyze the butyl titanate. Once SiO₂

99 was evenly dispersed, it was transferred to an autoclave with polytetrafluoroethylene (PTFE) at 200 °C
100 for 2 h. The filtrate was then allowed to cool to room temperature and washed with water and ethanol
101 until it became clear, after which it was dried at 60 °C to obtain a catalyst powder. Composite catalysts
102 with different TiO₂ loads were then obtained (loading = mass of TiO₂/total mass of catalyst).

103 **2.2 Sample characterization**

104 TiO₂ nanoparticles, the TiO₂/SiO₂ composite catalyst, and the recovered (i.e., used in a reaction
105 cycle) catalysts were characterized to study their morphology, structure, photochemical properties, and
106 chemical stability.

107 2.2.1 Characterization by scanning electron microscopy (SEM)

108 Samples were characterized by SEM (20,000x, Hitachi S4800) and energy-dispersive X-ray
109 spectroscopy (EDS) (HORIBA 7593-H) to examine their morphology and microstructure.

110 2.2.2 Characterization by X-ray diffraction (XRD)

111 An X-ray diffractometer (XRD, Ultima IV Advanced Diffractometer, CuK α) was used to analyze
112 the crystal structure of the samples within a 10°–80° range at a 5°/min scanning speed. The samples
113 were then evaluated based on their characteristic peaks.

114 2.2.3 Characterization by UV-Vis differential reflectance spectroscopy (DRS)

115 The photocatalysts were then examined via the UV-Vis diffuse reflectance test using a
116 spectrophotometer (Lambda 750 S, 200–800 nm) and the results were used to evaluate the light
117 absorption performance of the catalysts.

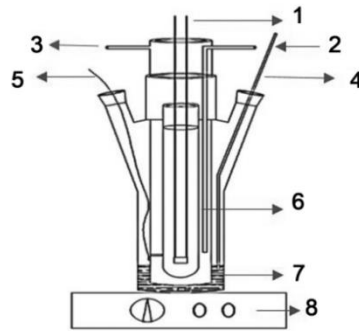
118 2.2.4 Characterization by Fourier infrared (FT-IR) spectroscopy

119 FT-IR tests were performed with a Bruker Vertex 70 FT-IR spectrophotometer within a 400–4000
120 nm wavelength range.

121 **2.3 Photocatalytic reduction of N-NO₃⁻**

122 A commercial glass photoreactor was used for the photocatalytic reduction of N-NO₃⁻, as shown
123 in Fig. 3. The experimental light source was a 125 w high-pressure mercury lamp with a primary
124 wavelength of 365 nm, and the device was equipped with an external water cooling system to ensure a

125 constant reaction temperature. For each experiment, 500 mL of KNO_3 ($C_0 = 30 \text{ mgN/L}$) solution was
 126 added to the reactor, after which predetermined amounts of catalyst and hole scavenger (formic acid)
 127 were sequentially added with constant stirring. The reaction solution was continuously purged with
 128 shielding gas to eliminate the oxygen from the device. The UV lamp was turned on 30 min prior to the
 129 experiment, after which the reaction solution was collected with a syringe every hour and filtered
 130 through a $0.22 \mu\text{m}$ membrane. The concentrations of ammonia nitrogen, nitrate nitrogen, and nitrite
 131 nitrogen were then measured separately. Higher removal rates and superior catalytic performance were
 132 obtained at lower N-NO_3^- residual concentrations. Further, higher N_2 production and selectivity were
 133 observed at lower ammonia nitrogen and nitrite nitrogen production levels.



134
 135 Fig. 1 Photocatalytic reaction setup: (1) UV light source; (2) water inlet; (3) water outlet; (4) air pump;
 136 (5) sampling port; (6) quartz cold trap; (7) reaction solution; (8) magnetic stirrer

137 2.4 Determination of indicators

138 2.4.1 Measurement of indicators

139 N-NO_3^- was determined via dual-wavelength UV spectrophotometry (HJ/T 346-2007), nitrite
 140 nitrogen was determined via N-(1-naiyl)-ethylenediamine spectrophotometry (GB 7493-87), and
 141 ammonia nitrogen was determined via Nessler's reagent spectrophotometry (HJ 535-2009).

142 2.4.2 N_2 removal rate and conversion rate calculations

$$143 \quad \text{N-NO}_3^- \text{ removal rate} = (C_0 - C_1) / C_0 \times 100\% \quad (2.4.2-1)$$

$$144 \quad \text{N}_2 \text{ selectivity} = (C_0 - C_1 - C_2 - C_3) / (C_0 - C_1) \times 100\% \quad (\text{N}_2 \text{ selectivity refers to the proportion of N}_2 \text{ in}$$

$$145 \quad \text{the product}) \quad (2.4.2-2)$$

146 where C_0 refers to the initial N-NO_3^- concentration in the solution; C_1 , C_2 , C_3 represent the

147 concentrations of N-NO_3^- , ammonia nitrogen, and nitrite nitrogen after the reaction, respectively.

148 **3 Results and Discussion**

149 **3.1 Sample characterization**

150 3.1.1 Crystal structure

151 The crystal structures of catalysts before and after the reactions were investigated by XRD and
152 FT-IR. Figs. 2 and 3 illustrate the XRD and FT-IR spectra of the catalysts before and after the reactions,
153 respectively. As shown in Fig. 2, the diffraction angle (2θ) of the sample in the 10° – 80° range was
154 consistent with the spectra of anatase TiO_2 (JCPDS No. 21-1272). Further, the 2θ diffraction peaks at
155 26.7° , 36.6° , 47.98° , 53.2° , 54.04° , and 62.86° ($\text{TiO}_2/\text{SiO}_2$ at $2\theta = 25.44^\circ$, 38.1° , 48.16° , 54.72° , 55.16° ,
156 and 63.0°) correspond to the (101), (004), (200), (105), (211), (204) crystalline surfaces of anatase TiO_2 ,
157 respectively, indicating that TiO_2 in the as-prepared composite maintained the anatase structure (Li et al.
158 2018, Yu et al. 2014).

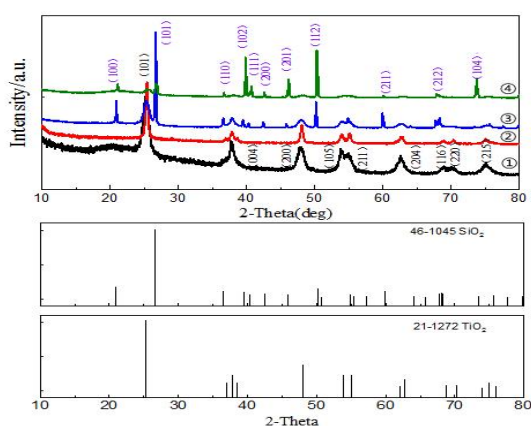
159 The peak shapes and peak positions of the XRD spectra of the catalysts before and after the
160 reactions were largely equal, and the crystalline structure of anatase did not change, indicating that the
161 structure of the catalysts prepared by this method did not change significantly before and after the
162 reactions. However, some of the reactants adsorbed on the sample surface during the reaction process
163 weakened the intensity of some characteristic peaks after the reaction.

164 As illustrated in Fig. 3, the catalysts exhibited IR absorption peaks at 3343, 1632, 1435, 1061, and
165 933 cm^{-1} before and after the reactions. The absorption peak at 3343 cm^{-1} corresponded to the O-H
166 bond stretching vibrations caused by water and hydroxyl groups adsorbed on the TiO_2 surface, whereas
167 the peaks at 1632, 1435, and 443 cm^{-1} were characteristic of TiO_2 . The very weak Ti-O-Si absorption
168 peaks of SiO_2 at 1061 and 933 cm^{-1} indicated that TiO_2 and SiO_2 were mainly physically bound (i.e., as
169 opposed to chemically bound), which mainly changed the physical properties of the catalysts. However,
170 the introduction of SiO_2 weakened the TiO_2 peak (Najafidoust et al. 2019, Yao et al. 2020).

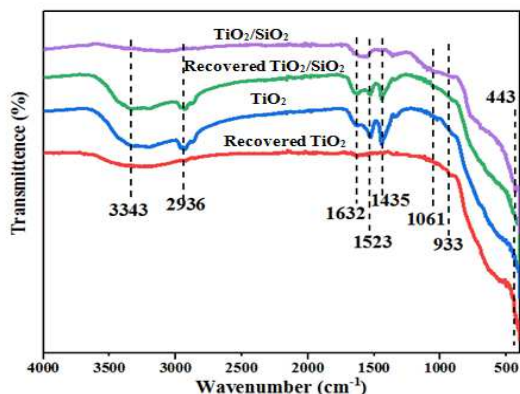
171 The grain size of the catalysts was calculated using the Debye-Scherrer Equation:

$$172 \quad D = k\lambda / [\cos\theta(\beta \div 180) \times 3.14] \quad (3.1.1-1)$$

173 where k is the Scherrer constant (the cubic particle constant k is 0.943), λ is the Cu κ 1 incident
 174 wavelength ($\lambda = 0.15406$ nm), θ is the diffraction angle, and β is the full half-maximum width. The full
 175 half-maximum width was calculated in radians and the strongest diffraction peak (101) of the catalysts
 176 was used to calculate the grain size. Table 3 summarizes the results of these calculations. Smaller
 177 catalyst grains possess a larger specific surface area and therefore have better photocatalytic
 178 performance and stronger redox ability (Lucchetti et al. 2017). Similarly, the electrons photogenerated
 179 by TiO₂ reach the catalyst surface more quickly when the catalyst grains are smaller, which reduces the
 180 electron-hole recombination rates and improves catalytic performance (Satayeva et al. 2018). Similarly,
 181 the solubility of the recovered catalysts increased due to the quantum size, and the catalytic
 182 performance was reduced by recrystallization in water during use, which led to an increase in crystal
 183 size.



184
 185 Fig. 2 XRD spectra of ①TiO₂, ②recovered TiO₂, ③ TiO₂/SiO₂, ④ recovered TiO₂/SiO₂, and TiO₂ compared
 186 to the XRD standard spectra of SiO₂



187
 188 Fig. 3 FT-IR spectra of TiO₂, recovered TiO₂, TiO₂/SiO₂, and recovered TiO₂/SiO₂ at 400–4000 cm⁻¹

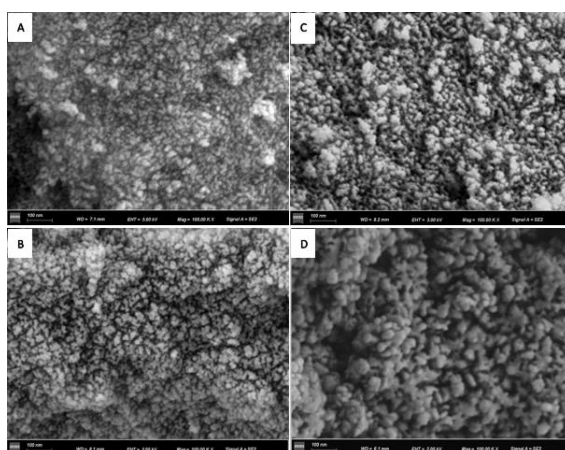
Table 1 Catalyst grain sizes

Photocatalyst	β	θ (°)	Size (nm)
TiO ₂	0.987	12.612	8.7
recovered TiO ₂	0.976	12.675	9.4
TiO ₂ /SiO ₂	1.048	12.726	7.8
recovered TiO ₂ /SiO ₂	0.947	12.605	8.6

190 3.1.2 Morphology and structure

191 The morphology and microstructure of the catalysts were investigated by SEM. Fig. 4(a) A-D
 192 shows representative SEM images (10000x) of TiO₂, recovered TiO₂, TiO₂/SiO₂, and recovered
 193 TiO₂/SiO₂, respectively. As illustrated in the figure, the catalysts exhibited spherical structures with
 194 heterogeneous sizes, and the recovered catalyst particles were slightly larger (Nguyen & Nguyen 2009).
 195 The elemental composition of the samples was determined via EDS mapping, and these results further
 196 confirmed whether the composite was successfully synthesized. As shown in Fig. 6 (b) and (c), Ti and
 197 O were uniformly distributed in TiO₂, whereas Ti, Si, and O were uniformly distributed in TiO₂/SiO₂.

198 The SEM images of samples demonstrated that the two catalysts were spherical in shape and
 199 similar in size both before and after the reactions. This was consistent with the results of XRD and the
 200 Debye-Scherrer Equation calculations, which further validated the stability of the samples.

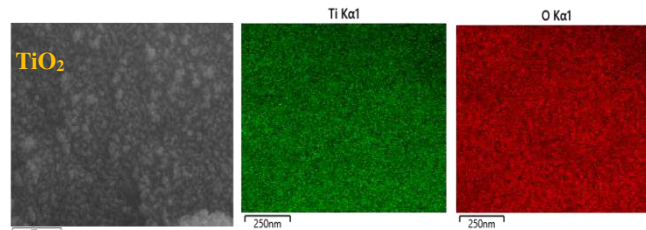


(a) SEM

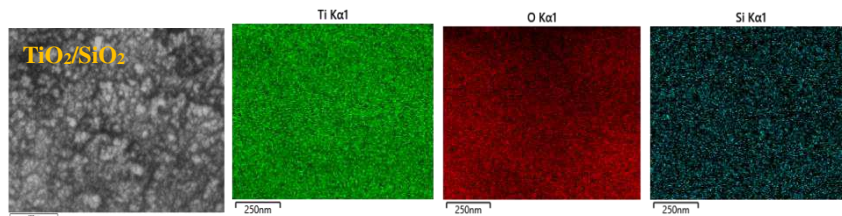
201

202

203



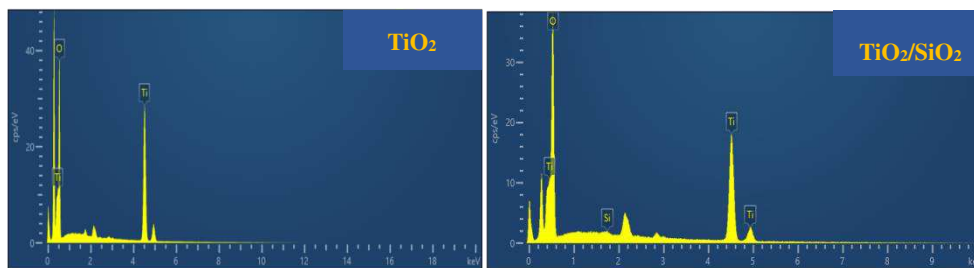
204



205

(b) Mapping

206



207

(c) EDS spectra

208

Fig. 4 (a; A-D) Representative SEM images (10000x) of TiO₂, recovered TiO₂, TiO₂/SiO₂, and recovered

209

TiO₂/SiO₂, respectively; (b) elemental mapping of the two samples; (c) EDS spectra of the two samples

210

3.1.3 Optical performance and band gap energy

211

The optical performance of a photocatalyst is a key feature that directly affects the photocatalytic

212

activity of the materials. Fig. 5 (a) shows the UV-Vis DRS absorption spectra of TiO₂, recovered TiO₂,

213

TiO₂/SiO₂, and recovered TiO₂/SiO₂ within a 200–800 nm range. Upon comparing the UV absorption

214

curves of TiO₂ and TiO₂/SiO₂, we observed that the peak UV light absorption occurred at

215

approximately 350 nm for both. However, TiO₂/SiO₂ had a stronger optical response to UV light, and

216

the absorption band was shifted to the long-wave direction.

217

The band gap energy was calculated as described in previous studies (Liu et al. 2018, Sun et al.

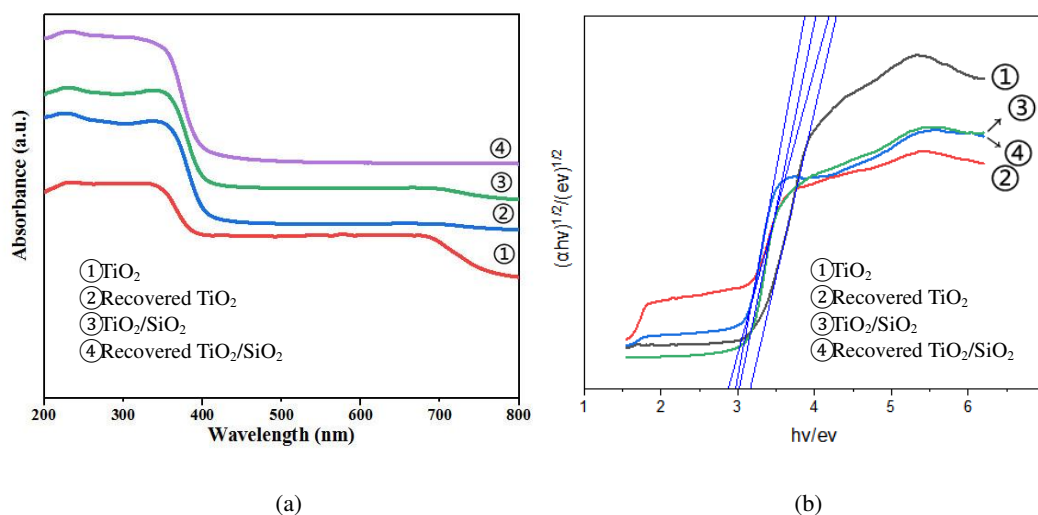
218

2013, Zhou et al. 2011):

219

$$(\alpha h\nu)^n = B(h\nu - E_g) \quad (3.1.3-1)$$

220 where $h\nu$ is the photon energy, E_g is the optical band gap of the semi-conductor, α is the absorption
 221 coefficient obtained from the scattering and reflection spectra according to Kubelka-Munk theory, B is
 222 the proportionality constant, and the value of n depends on the semi-conductor, as well as the type of
 223 transition. Fig. 7(b) shows the band gap energy of TiO_2 , recovered TiO_2 , $\text{TiO}_2/\text{SiO}_2$, and recovered
 224 $\text{TiO}_2/\text{SiO}_2$. As illustrated in the figure, the band gap energy of TiO_2 was 3.17 eV, whereas the band gap
 225 energy of $\text{TiO}_2/\text{SiO}_2$ was approximately 2.88 eV, which was consistent with previous results. The band
 226 gap energy of TiO_2 and $\text{TiO}_2/\text{SiO}_2$ increased slightly after use, and the increase in band gap energy
 227 indicated that the energy required for the electron transition also increased. This weakened UV light
 228 absorption and light utilization ability, and ultimately decreased the catalytic ability of the catalysts,
 229 which was consistent with the theory of UV absorption (Zhou et al. 2017).



230
 231 (a) (b)
 232 Fig. 5 (a) UV-Vis DRS spectra of TiO_2 , recovered TiO_2 , $\text{TiO}_2/\text{SiO}_2$, and recovered $\text{TiO}_2/\text{SiO}_2$ at 200–800 nm; (b)
 233 band gap energy evaluated by the Kubelka-Munk equation

234 3.2 Effects of different factors on N-NO_3^- removal rates

235 To investigate the influence of key factors on the removal rate of nitrates, two different gradients
 236 of each factor were selected for the orthogonal test, and the results are summarized in Table 2. The
 237 influencing factors exhibited the following order: N-NO_3^- concentration > TiO_2 dose > formic acid dose.
 238 A gradient test was then conducted according to the degree of influence of each factor.

239

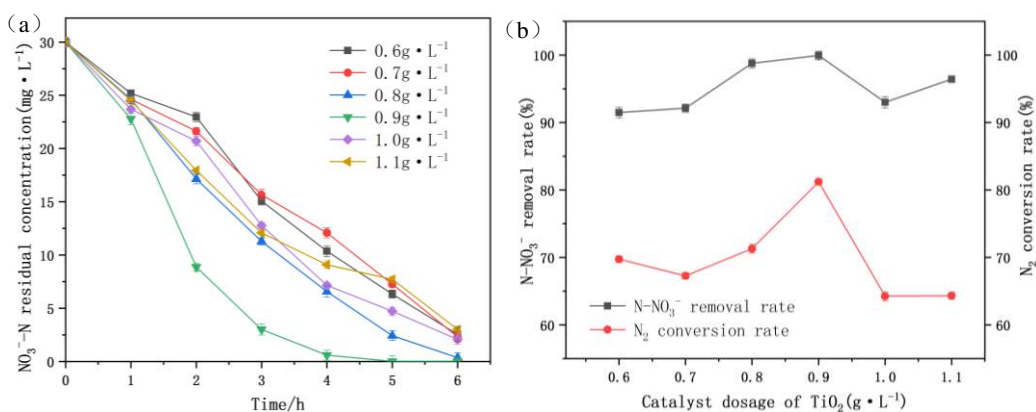
Table 2. Results of orthogonal tests of N-NO₃⁻ degradation catalyzed by TiO₂

Sample No.	Nitrate nitrogen concentration (mg·L ⁻¹)	Formic acid dose (mL·L ⁻¹)	TiO ₂ dose (g·L ⁻¹)	Nitrate nitrogen removal rate (%)
1	50	0.5	0.5	91
2	50	1.0	1.0	93
3	90	0.5	1.0	73
4	90	1.0	0.5	53
Mean 1 (%)	92	82	72	
Mean 2 (%)	63	83	73	
Range	0.29	0.09	0.11	

241 3.2.1 Effects of TiO₂ dose on the removal of low-concentration N-NO₃⁻

242 Fig. 6 shows the effects of TiO₂ dose (0.6, 0.7, 0.8, 0.9, 1.0, and 1.1 g·L⁻¹) on the removal of 30
 243 mg·L⁻¹ N-NO₃⁻ (formic acid dose = 0.6 mL·L⁻¹, CO₂ flow rate = 0.1 m³·h⁻¹). As illustrated in Fig. 6, the
 244 removal rate of N-NO₃⁻ exhibited an upward and then a downward trend with increasing TiO₂ doses.
 245 Further, the N-NO₃⁻ removal rate and N₂ selectivity in the products reached the highest values (99.93%
 246 and 81.21%, respectively) when the TiO₂ dose was 0.9 g·L⁻¹. As shown in Fig. 8 (a), the reaction rate
 247 reached a maximum at a TiO₂ dose of 0.9 g·L⁻¹.

248 Theoretically, higher catalyst concentrations should increase the availability of electrons and free
 249 radicals and, in turn, N-NO₃⁻ removal rates should continue to increase. However, catalytic
 250 performance decreased once the catalyst concentration reached a certain threshold, and similar results
 251 have been reported in several previous studies (Baniasadi et al. 2013, Sun et al. 2015). When the
 252 catalyst concentration was low, N-NO₃⁻ molecules were not in full contact with it and the catalytic
 253 efficiency was low. In contrast, when the catalyst concentration exceeded a critical level, the light
 254 transmittance in the solution decreased as the concentration increased, resulting in sub-optimal light
 255 utilization and a decrease in catalytic efficiency (Peng et al. 2018, Sun et al. 2015).



256

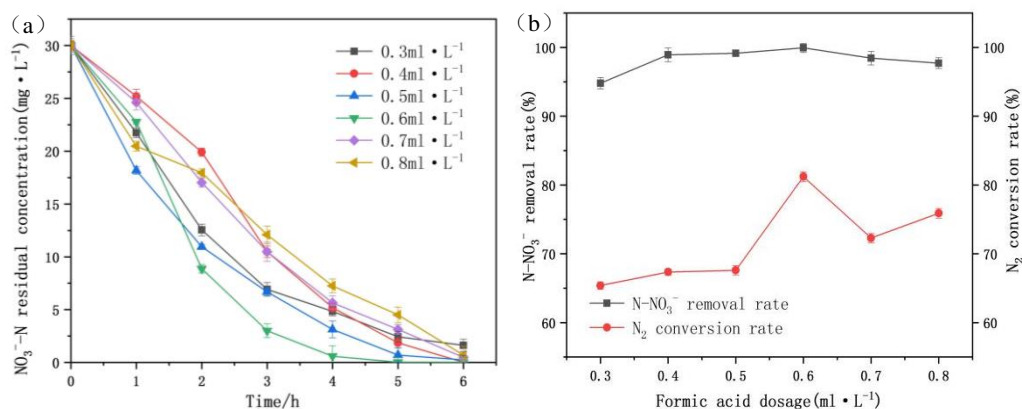
257 Fig. 6 (a) Effects of TiO_2 dose on N-NO_3^- photocatalytic reduction as a function of time; (b) effects of
 258 catalyst dosage on N-NO_3^- removal rate and N_2 selectivity in the products

259 3.2.2 Effects of formic acid dose on the removal rates of low-concentration N-NO_3^-

260 In this reaction, formic acid was used as the hole scavenger, and appropriate amounts of formic
 261 acid were added to improve the efficiency of the reaction. The N-NO_3^- removal rate was only 11.9% in
 262 the experimental group without formic acid. Fig. 7 illustrates the effects of formic acid dose (0.3, 0.4,
 263 0.5, 0.6, 0.7, and 0.8 $\text{mL} \cdot \text{L}^{-1}$) on the removal rate of $30 \text{ mg} \cdot \text{L}^{-1}$ N-NO_3^- (TiO_2 dose = $0.9 \text{ g} \cdot \text{L}^{-1}$, CO_2
 264 flow rate = $0.1 \text{ m}^3 \cdot \text{h}^{-1}$). As shown in Fig. 7, the N-NO_3^- removal rate first increased and then decreased
 265 with increasing formic acid concentration, and the N_2 selectivity in the products first increased and then
 266 stabilized. Further, both the N-NO_3^- removal rate and N_2 selectivity in the products reached maximum
 267 levels (99.93% and 81.21%, respectively) when the formic acid dose was $0.6 \text{ mL} \cdot \text{L}^{-1}$ [Fig. 7 (a)]. The
 268 reaction rate reached its maximum in the first 4 h and then slowed down as the reactant concentrations
 269 decreased.

270 The role of the hole scavenger in the photocatalytic reactions was to improve photocatalytic
 271 efficiency by irreversibly binding to the catalyst surface and preventing complexation with holes.
 272 Formic acid, a weak acid, had a weaker adsorption capacity with TiO_2 than nitrate ions. Formic acid
 273 and holes (h^+) reacted to produce $\cdot\text{CO}_2^-$, which in turn promoted further N_2 production (Chu
 274 & Anastasio 2003, Mack & Bolton 1999). Catalytic efficiency gradually increased with the addition of
 275 formic acid because the complexation of electrons and holes was prevented. However, excessive formic
 276 acid addition increased the number of formic acid molecules, and therefore these molecules were more
 277 likely to collide with the catalyst surface than the nitrate ions, thus decreasing catalytic efficiency

278 (Caswell et al. 2020).



279

280 Fig. 7 (a) Effects of formic acid dose on N-NO_3^- photocatalytic reduction as a function of time; (b)

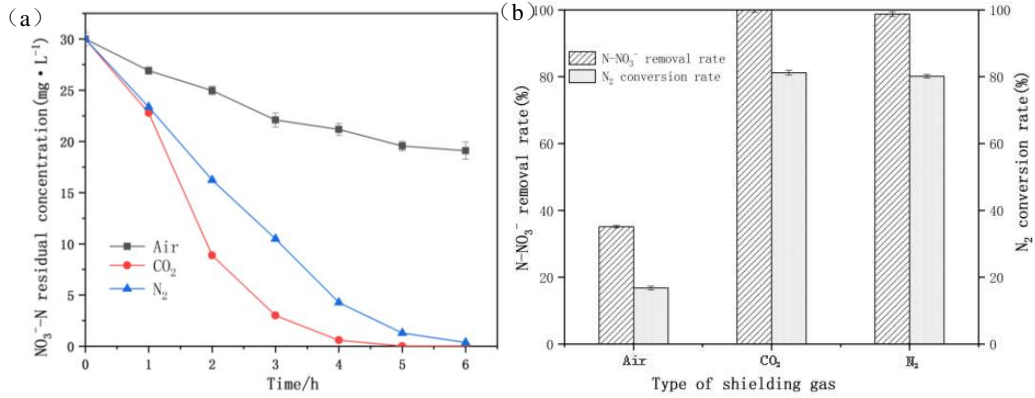
281 effects of formic acid dose on N-NO_3^- removal rate and N_2 selectivity in the products

282 3.2.3 Effects of different types of shielding gas on low-concentration N-NO_3^- removal rates

283 Fig. 8 shows the effects of different types of shielding gas (CO_2 , N_2 , air) on the removal rate of 30
284 $\text{mg} \cdot \text{L}^{-1}$ N-NO_3^- (formic acid dose = 0.6 $\text{mL} \cdot \text{L}^{-1}$, TiO_2 dose = 0.9 $\text{g} \cdot \text{L}^{-1}$, aeration rate = 0.1 $\text{m}^3 \cdot \text{h}^{-1}$). As
285 indicated in the figure, the removal rates of N-NO_3^- were 98.76% and 99.93% and N_2 selectivity in the
286 products were 80.14% and 81.21% under protection by N_2 and CO_2 , respectively, indicating that CO_2
287 was superior to N_2 in this case, although the difference was relatively subtle.

288 Nitrate removal is a reduction reaction, and shielding gas is introduced to remove dissolved
289 oxygen from water and create a reduction environment in the closed reactor. Interestingly, the results of
290 the air aeration experiment confirmed this notion. CO_2 is more effective than N_2 because the pH of the
291 N_2 -aerated solution is close to neutral under this reaction condition, whereas CO_2 dissolved in water
292 can produce H^+ . Photocatalytic reduction of nitrates requires the consumption of H^+ , and therefore this
293 reaction is more effective under weakly acidic conditions (Ren et al. 2015).

294



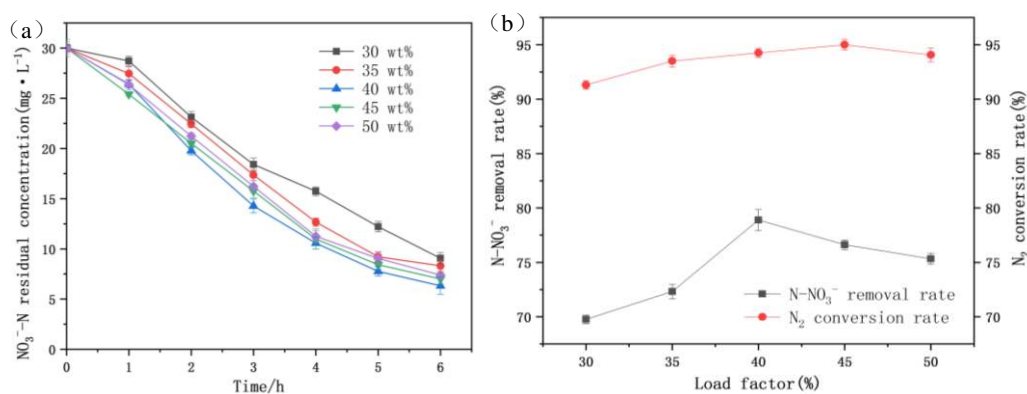
295

296 Fig. 8 (a) Effects of type of shielding gas on N-NO₃⁻ photocatalytic reduction as a function of time; (b) effects of
 297 type of shielding gas on the N-NO₃⁻ removal rate and N₂ selectivity in the products

298 3.2.4 Effects of TiO₂/SiO₂ loading on N-NO₃⁻ removal rates in low-concentration solutions

299 Fig. 9 shows the effects of different TiO₂/SiO₂ loads (30%, 35%, 40%, 45%, 50%) on the removal
 300 rate of 30 mg·L⁻¹ N-NO₃⁻ (formic acid dose = 0.6 mL·L⁻¹, TiO₂/SiO₂ dose = 1.5 g·L⁻¹, CO₂ flow rate =
 301 0.1 m³·h⁻¹). As illustrated in Fig. 9, as the loading rate increased from 30% to 50%, the removal rate of
 302 N-NO₃⁻ increased first and then decreased to a relatively stable level. The maximum N-NO₃⁻ removal
 303 rate (78.89%) was achieved with a TiO₂/SiO₂ load of 40%, and the N₂ conversion rate was 94.25%

304 At low loading rates, the amount of TiO₂ increased with higher loading rates, thus increasing the
 305 number of active sites of the catalyst, as well as the likelihood of contact between nitrate ions and the
 306 catalyst. Further, catalytic efficiency also increased at higher loading rates but then decreased with
 307 additional loading rate increases after reaching a peak. This was because too much TiO₂ accumulated
 308 on the SiO₂ surface, which was not conducive for dispersion. The specific surface area decreased and
 309 catalytic performance also decreased accordingly (Cai et al. 2018). Further, excessively high doping
 310 amounts resulted in decreases in the effective active sites in the center, as well as light energy
 311 utilization rates and catalytic efficiency.



312

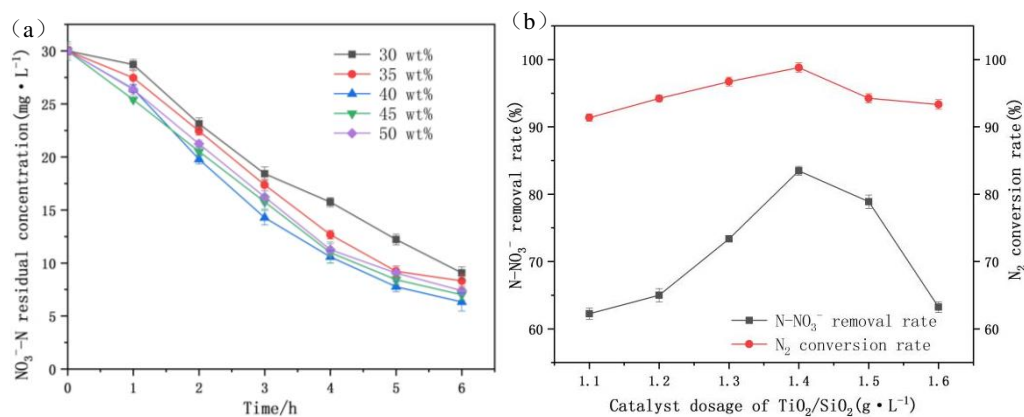
313 Fig. 9 (a) Effects of $\text{TiO}_2/\text{SiO}_2$ loading on N-NO_3^- photocatalytic reduction as a function of time; (b) effects of
 314 $\text{TiO}_2/\text{SiO}_2$ on N-NO_3^- removal rate and N_2 selectivity in the products

315 3.2.5 Effects of $\text{TiO}_2/\text{SiO}_2$ dose on N-NO_3^- removal rate in low-concentration solutions

316 The effect of different $\text{TiO}_2/\text{SiO}_2$ composite catalyst doses (1.1, 1.2, 1.3, 1.4, 1.5, and 1.6 $\text{g} \cdot \text{L}^{-1}$)
 317 with 40% loading on the photocatalytic degradation of 30 $\text{mg} \cdot \text{L}^{-1}$ N-NO_3^- was investigated at a formic
 318 acid dose of 0.6 $\text{mL} \cdot \text{L}^{-1}$ and a CO_2 flow rate of 0.1 $\text{m}^3 \cdot \text{h}^{-1}$. As shown in Fig. 10, the removal rate of
 319 N-NO_3^- and conversion rate of ammonia nitrogen increased higher $\text{TiO}_2/\text{SiO}_2$ doses and then decreased
 320 after reaching a peak. Both the N-NO_3^- removal rate and conversion rate reached a maximum (83.48%
 321 and 98.80%, respectively) when the $\text{TiO}_2/\text{SiO}_2$ dose was 1.4 $\text{g} \cdot \text{L}^{-1}$.

322 The N-NO_3^- removal rate and N_2 selectivity in the products increased with higher doses due to
 323 increases in TiO_2 concentrations. Specifically, this increase in the concentration of effective catalysts
 324 could improve light utilization, resulting in an excellent removal effect. However, as these doses
 325 increased further, the N-NO_3^- removal rate and N_2 selectivity in the products decreased due to the effect
 326 of gravity on SiO_2 , which caused the deposition of the composite catalyst and reduced light utilization,
 327 and therefore catalytic efficiency was slightly decreased (Wang et al. 2021).

328



329

330 Fig. 10 (a) Effects of TiO₂/SiO₂ dose on N-NO₃⁻ photocatalytic reduction as a function of time; (b) effects of the

331

TiO₂/SiO₂ dose on N-NO₃⁻ removal rate and N₂ selectivity in the products

332

3.3 Sample stability

333

Catalyst stability is another important parameter to evaluate when assessing catalytic performance.

334

To achieve this, the reacted catalyst was recovered and tested several times under the same conditions.

335

After the reaction, the reaction system was allowed to stand and was then filtered. Our findings

336

indicated that the recovery effect of TiO₂/SiO₂ was superior to that of TiO₂. The filtered catalyst was

337

repeatedly washed with water and dried in an oven at 60 °C for reuse. Under optimal conditions (initial

338

N-NO₃⁻ concentration of 30 mg·L⁻¹, formic acid dose of 0.6 mL·L⁻¹, CO₂ flow rate of 0.1 m³·h⁻¹, TiO₂

339

dose of 0.9 g·L⁻¹, 40 wt% TiO₂/SiO₂ dose of 1.4 g·L⁻¹) The experiments were repeated three times and

340

the results are shown in Fig. 11. The catalytic efficiency of the two catalysts decreased after

341

reapplication, indicating that the photocatalytic performance of the used catalysts was reduced. Further,

342

the particle size of both catalysts increased after use, which affected light utilization and decreased

343

catalytic efficiency. The difference in the catalytic efficiency of TiO₂ from 99.93% in the first use cycle

344

to 72.38% in the second cycle was very significant, whereas the difference between the third and fourth

345

cycles was not significant, both of which accounted for approximately 65% of the removal efficiency

346

of the first cycle. This was because TiO₂ tended to agglomerate after use, which reduced its specific

347

surface area and catalytic efficiency. The catalytic efficiency of TiO₂/SiO₂ decreased from 83.48% in

348

the first cycle to 76.43% in the second cycle. Similar to TiO₂, the difference in the removal rate

349

between the third and fourth cycles was not significant, both of which accounted for approximately

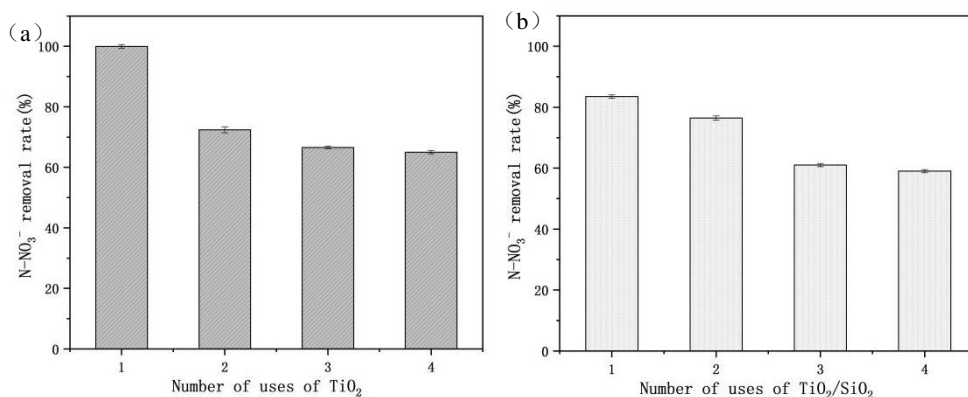
350

73% of the removal efficiency of the first cycle. Given that TiO₂ and SiO₂ were only physically bound,

351

repeated washing would cause some of TiO₂ to fall off from SiO₂, thus decreasing the effective catalyst

352 concentration and the overall catalytic efficiency.



353

354 Fig. 11 (a) Effect of the number of TiO₂ utilization cycles on N-NO₃⁻ removal rates; (b) effect of the number of
355 TiO₂/SiO₂ utilization cycles on N-NO₃⁻ removal rates

356 3.4 Mechanism of N-NO₃⁻ photocatalytic reduction

357 3.4.1 Kinetics of photocatalytic reduction of nitrates

358 In photocatalysis studies, the kinetics of photocatalytic reactions are commonly analyzed by the
359 Langmuir-Hinshelwood kinetic equations:

$$360 \quad r = \frac{1}{V} \frac{dC}{dt} = \frac{kC}{1+(kC)^2} \quad (3.4.1-1)$$

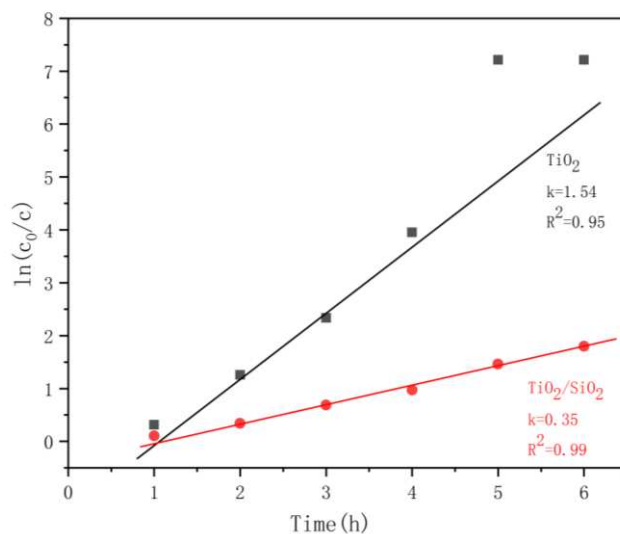
361 Given that the reaction kinetics of the photocatalytic reduction of nitrates follows the first-order
362 reaction kinetic model, the Langmuir-Hinshelwood kinetic equation can be changed as follows:

$$363 \quad \ln \frac{C}{C_0} = -kt \quad (3.4.1-2)$$

364 where C₀ refers to the initial concentration of ammonia nitrogen in the solution, C refers to the
365 concentration of ammonia nitrogen at any given moment, and k refers to the kinetic constant.

366 As shown in Fig. 12, the concentration of nitrates was linearly related to the reaction time, and the
367 correlation coefficients of TiO₂ and TiO₂/SiO₂ reached 0.95 and 0.99, respectively, indicating that the
368 photocatalytic reduction of N-NO₃⁻ was consistent with the first-order reaction. The kinetic constant of
369 TiO₂ was 4.4 times higher than that of TiO₂/SiO₂. Therefore, TiO₂ was more effective than TiO₂/SiO₂
370 for the photocatalytic reduction of nitrates. Nevertheless, TiO₂/SiO₂ had a higher N₂ selectivity and

371 could be easily recycled.



372

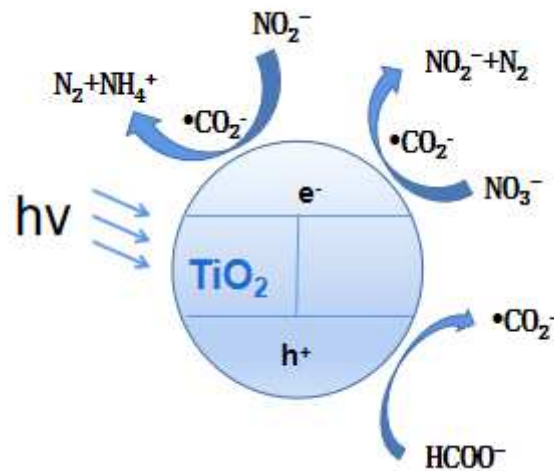
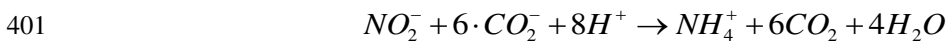
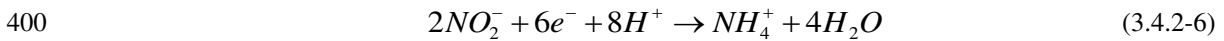
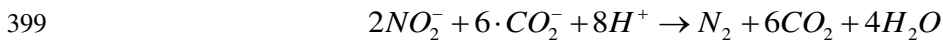
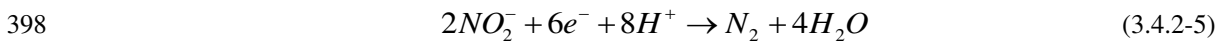
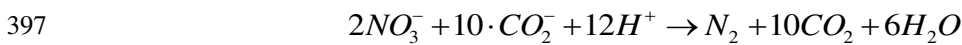
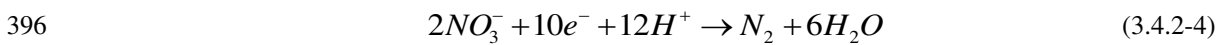
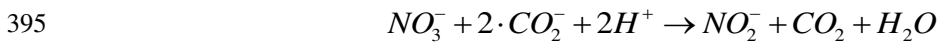
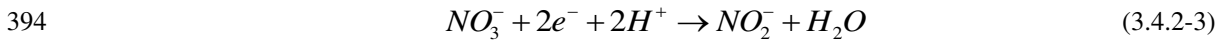
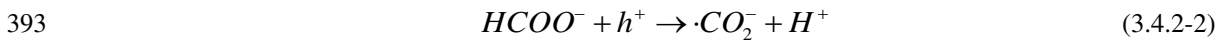
373 Fig. 12 First-order kinetic model of the photocatalytic oxidation of ammonia nitrogen by TiO₂ and
374 TiO₂/SiO₂

375 3.4.2 Mechanism of photocatalytic reduction of nitrates

376 Based on the results of this study and previous studies of photocatalysis by TiO₂, we proposed the
377 potential mechanisms of photocatalytic reduction of N-NO₃⁻ by TiO₂ (Fig. 13).

378 TiO₂ had a low-energy valence band and a high-energy conduction band, which were
379 discontinuous and separated by a band gap. The electrons occupied the low-energy valence band and
380 the high-energy conduction band was empty. When the incident light intensity was greater than or
381 equal to the width of the band gap, the excited electrons in the valence band migrated to the conduction
382 band, generating negatively charged electrons (e⁻) in the conduction band and a hole (h⁺) in the valence
383 band (Pawar et al. 2018). The photogenerated electrons and holes were separated by an electric field
384 and migrated to the catalyst surface, where the holes (h⁺) combined with the formic acid on the catalyst
385 surface to generate free radicals ($\cdot\text{CO}_2^-$). The photogenerated electrons and $\cdot\text{CO}_2^-$ were highly reductive
386 and contributed to the degradation of N-NO₃⁻ and the further conversion of intermediates to N₂ (Chu
387 & Anastasio 2003, Mack & Bolton 1999). NO₃⁻ was reduced to N₂ and NO₂⁻ (Eqs. 3.4.2-3-3.4.2-4) on
388 the catalyst surface by the photogenerated electrons and $\cdot\text{CO}_2^-$, and NO₂⁻ on the catalyst surface was
389 reduced to N₂ (Eq 3.4.2-5) or NH₄⁺ (Eq 3.4.2-6) in the presence of photogenerated electrons and $\cdot\text{CO}_2^-$
390 (Wang et al. 2021). The main product of the reaction was N₂, whereas NO₂⁻ and NH₄⁺ were produced in

391 trace amounts, which was consistent with previous studies (Doudrick et al. 2012, Ren et al. 2015).



402

403 Fig. 13 Mechanism of photocatalytic reduction of N-NO₃⁻ by TiO₂

404 5 Conclusions

405 TiO₂ exhibited an excellent effect on the photocatalytic reduction of N-NO₃⁻ in water. However, to
 406 enhance its recoverability and recyclability, a TiO₂/SiO₂ composite catalyst was prepared by loading
 407 TiO₂ on SiO₂. The components in the TiO₂/SiO₂ composite catalyst were evenly distributed, and the

408 two were mainly physically bound. This composite catalyst exhibited smaller TiO_2 particles on its
409 surface, which increased its specific surface area and improved light utilization. After the conjugation
410 of these two agents, their structure remained largely unchanged; however, the adsorption of the
411 reactants resulted in a larger crystal size, which reduced the catalytic performance. Further, the
412 recovery test demonstrated that the catalyst stability could still be further improved.

413 TiO_2 was more effective in treating low-concentration N-NO_3^- wastewater, whereas $\text{TiO}_2/\text{SiO}_2$ was
414 more effective in treating medium-concentration N-NO_3^- wastewater. Moreover, the selectivity of N_2 in
415 the products of $\text{TiO}_2/\text{SiO}_2$ was higher than that of TiO_2 . In the photocatalytic reduction of N-NO_3^- , both
416 e^- and $\cdot\text{CO}_2^-$ could reduce N-NO_3^- , and NO_3^- could be reduced to N_2 , NO_2^- , and NH_4^+ ; however, NO_2^-
417 and NH_4^+ occurred in trace amounts, and the final product was mostly N_2 .

418 **Declarations**

419 **Ethics approval and consent to participate**

420 Not applicable.

421 **Consent for publication**

422 Informed consent was obtained from all individual participants included in the study.

423 **Availability of data and materials**

424 All data generated or analysed during this study are included in this published article [and its
425 supplementary information files].

426 **Competing interests**

427 The authors declare that they have no competing interests.

428 **Authors' contributions**

429 **Wanzhen Zhong**:Conceptualization, Methodology, Writing - Original Draft.

430 **Weizhang Fu***: Supervision, Project administration.

431 **Shujuan Sun***: Writing - review & editing.

432 **Lingsheng Wang**: Investigation, Software, Resources.

433 **Huaihao Liu**: Validation, Formal analysis.

434 **Junzhi Wang**:Data Curation, Visualization.

435 ***Weizhang Fu and Shujuan Sun** are contributed equally to this work,both corresponding authors.

436 **Acknowledgements**

437 This work was supported by the National Natural Science Foundation [grant number U1906219],
438 Shandong Province major scientific and technological innovation project[grant number
439 2019JZZY010723], Natural Science Foundation of Shandong Province[grant number ZR2020MB087].

440 **References**

- 441 Baniasadi E, Dincer I, Naterer GF (2013): Measured effects of light intensity and catalyst concentration
442 on photocatalytic hydrogen and oxygen production with zinc sulfide suspensions.
443 International Journal of Hydrogen Energy 38, 9158-9168
- 444 Bi X, Du G, Kalam A, Sun D, Zhao W, Yu Y, Su Q, Xu B, Al-Sehemi AG (2021): Constructing anatase
445 TiO₂/Amorphous Nb₂O₅ heterostructures to enhance photocatalytic degradation of
446 acetaminophen and nitrogen oxide. Journal of Colloid and Interface Science 601, 346-354
- 447 Cai S, Shi S, Li H, Bai Y, Dang D (2018): Construction of self-sufficient Z-scheme Ag₃PW₁₂O₄₀/TiO₂
448 photocatalysts for the improved visible-light-driven photo-degradation of rhodamine B.
449 Research on Chemical Intermediates 44
- 450 Caswell T, Dlamini MW, Miedziak P, Pattison S, Davies P, Taylor S, Hutchings G (2020):
451 Enhancement in the rate of nitrate degradation on Au- and Ag-decorated TiO₂ photocatalysts.
452 Catalysis Science & Technology 10
- 453 Chu L, Anastasio C (2003): Quantum Yields of Hydroxyl Radical and Nitrogen Dioxide from the
454 Photolysis of Nitrate on Ice. The Journal of Physical Chemistry A 107, 9594-9602
- 455 Doudrick K, Monzon O, Mangonon A, Hristovski K, Westerhoff P (2012): Nitrate Reduction in Water
456 Using Commercial Titanium Dioxide Photocatalysts (P25, P90, and Hombikat UV100).
457 Journal of Environmental Engineering-Asce 138, 852-861
- 458 Gao Q, Wang C-Z, Liu S, Hanigan D, Liu S-T, Zhao H-Z (2019): Ultrafiltration membrane
459 microreactor (MMR) for simultaneous removal of nitrate and phosphate from water. Chemical
460 Engineering Journal 355, 238-246
- 461 Garcia-Segura S, Lanzarini-Lopes M, Hristovski K, Westerhoff P (2018): Electrocatalytic reduction of
462 nitrate: Fundamentals to full-scale water treatment applications. Applied Catalysis B:
463 Environmental, S0926337318304715
- 464 Ghafari S, Hasan M, Aroua MK (2008): Bio-electrochemical removal of nitrate from water and
465 wastewater—A review. Bioresource Technology 99, 3965-3974

466 Hou Z, Chu J, Liu C, Wang J, Li A, Lin T, François-Xavier CP (2021): High efficient photocatalytic
467 reduction of nitrate to N_2 by Core-shell $Ag/SiO_2@cTiO_2$ with synergistic effect of light
468 scattering and surface plasmon resonance. *Chemical Engineering Journal* 415, 128863

469 Jesus MAML, Ferreira AM, Lima LFS, Batista GF, Mambrini RV, Mohallem NDS (2021):
470 Micro-mesoporous TiO_2/SiO_2 nanocomposites: Sol-gel synthesis, characterization, and
471 enhanced photodegradation of quinoline. *Ceramics International* 47, 23844-23850

472 Li H, Cai S, Yang P, Bai Y, Dang D (2018): The synergistic effect of phase heterojunction and surface
473 heterojunction to improve photocatalytic activity of $VO\bullet-TiO_2$: the co-catalytic effect of
474 $H_3PW_{12}O_{40}$. *Journal of Nanoparticle Research* 20

475 Li X, Xiong J, Xu Y, Feng Z, Huang J (2019): Defect-assisted surface modification enhances the
476 visible light photocatalytic performance of $g-C_3N_4@C-TiO_2$ direct Z-scheme heterojunctions.
477 *Chinese Journal of Catalysis* 40, 424-433

478 Li X, Wang S, An H, Dong G, Feng J, Wei T, Ren Y, Ma J (2021): Enhanced photocatalytic reduction of
479 nitrate enabled by Fe-doped $LiNbO_3$ materials in water: Performance and mechanism. *Applied*
480 *Surface Science* 539, 148257

481 Liu W-X, Zhu X-L, Liu S-Q, Gu Q-Q, Meng Z-D (2018): Near-Infrared-Driven Selective
482 Photocatalytic Removal of Ammonia Based on Valence Band Recognition of an
483 $\alpha-MnO_2/N$ -Doped Graphene Hybrid Catalyst. *ACS Omega* 3, 5537-5546

484 Liu X, Liu H, Wang Y, Yang W, Yu Y (2021): Nitrogen-rich $g-C_3N_4@AgPd$ Mott-Schottky
485 heterojunction boosts photocatalytic hydrogen production from water and tandem reduction of
486 NO_3^- and NO_2^- . *Journal of Colloid and Interface Science* 581, 619-626

487 Lucchetti R, Siciliano A, Clarizia L, Russo D, Di Somma I, Natale F, Guida M, Andreozzi R, Marotta R
488 (2017): Sacrificial photocatalysis: removal of nitrate and hydrogen production by
489 nano-copper-loaded P25 titania. A kinetic and ecotoxicological assessment. *Environmental*
490 *Science and Pollution Research* 24

491 Lv T, Wang H, Hong W, Wang P, Jia L (2019): In situ self-assembly synthesis of sandwich-like
492 TiO_2 /reduced graphene oxide/ LaFeO_3 Z-scheme ternary heterostructure towards enhanced
493 photocatalytic hydrogen production. *Molecular Catalysis* 475, 110497

494 Mack J, Bolton JR (1999): Photochemistry of nitrite and nitrate in aqueous solution: a review. *Journal*
495 *of Photochemistry and Photobiology A: Chemistry* 128, 1-13

496 Najafidoust A, Haghghi M, Abbasi Asl E, Bananifard H (2019): Sono-solvothermal design of
497 nanostructured flowerlike BiOI photocatalyst over silica-aerogel with enhanced
498 solar-light-driven property for degradation of organic dyes. *Separation and Purification*
499 *Technology* 221, 101-113

500 Nguyen V-C, Nguyen T-V (2009): Photocatalytic decomposition of phenol over N-TiO₂-SiO₂ catalyst
501 under natural sunlight. *Journal of Experimental Nanoscience* 4, 233-242

502 Pawar M, Sengođular ST, Gouma P, Cozzoli PD (2018): A Brief Overview of TiO₂ Photocatalyst for
503 Organic Dye Remediation: Case Study of Reaction Mechanisms Involved in Ce-TiO₂
504 Photocatalysts System. 2018, 13

505 Peng X, Wang M, Hu F, Qiu F, Zhang T, Dai H, Cao Z (2018): Multipath fabrication of hierarchical
506 CuAl layered double hydroxide/carbon fiber composites for the degradation of ammonia
507 nitrogen. *Journal of environmental management* 220, 173-182

508 Ren H, Jia S-Y, Zou J-J, Wu S-H, Han X (2015): A facile preparation of Ag₂O/P25 photocatalyst for
509 selective reduction of nitrate. *Applied Catalysis B: Environmental* 176

510 Satayeva AR, Howell CA, Korobeinyk AV, Jandosov J, Inglezakis VJ, Mansurov ZA, Mikhalovsky SV
511 (2018): Investigation of rice husk derived activated carbon for removal of nitrate
512 contamination from water. *Science of The Total Environment* 630, 1237-1245

513 Sun D, Sun W, Yang W, Li Q, Shang JK (2015): Efficient photocatalytic removal of aqueous
514 NH_4^+ - NH_3 by palladium-modified nitrogen-doped titanium oxide nanoparticles under visible
515 light illumination, even in weak alkaline solutions. *Chemical Engineering Journal* 264,
516 728-734

517 Sun H, Zhou G, Liu S, Ang HM, Tadó MO, Wang S (2013): Visible light responsive titania
518 photocatalysts codoped by nitrogen and metal (Fe, Ni, Ag, or Pt) for remediation of aqueous
519 pollutants. *Chemical Engineering Journal* 231, 18-25

520 Takari A, Ghasemi AR, Hamadian M, Sarafrazi M, Najafidoust A (2021): Molecular dynamics
521 simulation and thermo-mechanical characterization for optimization of three-phase
522 epoxy/TiO₂/SiO₂ nano-composites. *Polymer Testing* 93, 106890

523 Tsang CHA, Li K, Zeng Y, Zhao W, Zhang T, Zhan Y, Xie R, Leung DYC, Huang H (2019): Titanium
524 oxide based photocatalytic materials development and their role of in the air pollutants
525 degradation: Overview and forecast. *Environment International* 125, 200-228

526 Tugaoen HON, Garcia-Segura S, Hristovski K, Westerhoff PJSOTTE (2017): Challenges in
527 photocatalytic reduction of nitrate as a water treatment technology. *Water Science and Technology* 77, 599–600, 1524-1551

528 Velu M, Balasubramanian B, Velmurugan P, Kamyab H, Ravi AV, Chelliapan S, Lee CT, Palaniyappan
529 J (2021): Fabrication of nanocomposites mediated from aluminium nanoparticles/Moringa
530 oleifera gum activated carbon for effective photocatalytic removal of nitrate and phosphate in
531 aqueous solution. *Journal of Cleaner Production* 281, 124553

532 Wang B, An B, Su Z, Li L, Liu Y (2021): A novel strategy for sequential reduction of nitrate into
533 nitrogen by CO₂ anion radical: Experimental study and DFT calculation. *Chemosphere* 269,
534 128754

535 Wang L, Fu W, Zhuge Y, Wang J, Yao F, Zhong W, Ge X (2021): Synthesis of polyoxometalates
536 (POM)/TiO₂/Cu and removal of nitrate nitrogen in water by photocatalysis. *Chemosphere* 278,
537 130298

538 Wang Y, Xing Z, Li Z, Wu X, Wang G, Zhou W (2017): Facile synthesis of high-thermostably ordered
539 mesoporous TiO₂/SiO₂ nanocomposites: An effective bifunctional candidate for removing
540 arsenic contaminations. *Journal of Colloid and Interface Science* 485, 32-38

541 Woottikrai C, Arisa S, Pimluck K, Yothin C (2022): Direct dye wastewater photocatalysis using
542 immobilized titanium dioxide on fixed substrate. *Chemosphere* 286

543 Yang Y, Li X-j, Chen J-t, Wang L-y (2004): Effect of doping mode on the photocatalytic activities of
544 Mo/TiO₂. Journal of Photochemistry and Photobiology A: Chemistry 163, 517-522

545 Yao F, Fu W, Ge X, Wang L, Wang J, Zhong W (2020): Preparation and characterization of a copper
546 phosphotungstate/titanium dioxide (Cu-H₃PW₁₂O₄₀/TiO₂) composite and the photocatalytic
547 oxidation of high-concentration ammonia nitrogen. Science of The Total Environment 727,
548 138425

549 Yu W, Liu X, Pan L, Li J, Liu J, Zhang J, Li P, Chen C, Sun Z (2014): Enhanced visible light
550 photocatalytic degradation of methylene blue by F-doped TiO₂. Applied Surface Science 319,
551 107-112

552 Zhou G, Sun H, Wang S, Ming Ang H, Tade MO (2011): Titanate supported cobalt catalysts for
553 photochemical oxidation of phenol under visible light irradiations. Separation and Purification
554 Technology 80, 626-634

555 Zhou G, Shen L, Xing Z, Kou X, Duan S, Fan L, Meng H, Xu Q, Zhang X, Li L, Zhao M, Mi J, Li Z
556 (2017): Ti³⁺ self-doped mesoporous black TiO₂/graphene assemblies for unpredicted-high
557 solar-driven photocatalytic hydrogen evolution. Journal of Colloid and Interface Science 505,
558 1031-1038

559